JASA ARTICLE

Sound power from a collection of monopoles with arbitrary coherence: Theory and application to aeroacoustic noise sources

Tyce W. Olaveson[a] and Kent L. Gee
Department of Physics and Astronomy, Brigham Young University, Provo, Utah 84602, USA

ABSTRACT:
Sound power is a fundamental characteristic of an acoustic source that is critical to developing radiation models. Current analytical methods for calculating sound power from a collection of monopoles either assume perfect coherence or incoherence. However, partially coherent sources are plentiful in structural acoustics and aeroacoustic applications. This paper expands the approach of Nelson, Curtis, Elliott, and Bullmore [(1987). J. Sound Vib. **116**, 397–414], who calculated sound power due to mutual coupling between coherent sources, to allow for partially coherent interactions. This expression is used to find the sound power from quadrupole-like source configurations with varying degrees of coherence. When calculating the sound power, partially coherent interactions are limited by two factors: a coupling distance and the coherence length. A numerical example of a driven plate is used to demonstrate the regions where the partially coherent sound power is most applicable. It is shown that when the system coherence length is larger than about one wavelength, the sound power can be calculated assuming a fully coherent source. A final example is shown for the T-7A jet at MIL and AB engine conditions. Sound power spectra are created from an equivalent source model of partially coherent monopoles and compared to measured far-field spectra.
 https://doi.org/10.1121/10.0042361
(Received 20 May 2025; revised 18 December 2025; accepted 9 January 2026; published online 2 February 2026)
[Editor: Lixi Huang] Pages: 1036–1047

I. INTRODUCTION

Sound power is a fundamental metric that quantifies the acoustic energy radiated by a noise source. It plays an important role in assessing the impact of noise and designing noise control strategies. To ensure consistency between measurements, both the International Organization for Standardization (ISO, 2019) and the American National Standards Institution (ANSI/ASA, 2012) have established guidelines for determining sound power levels (see ISO 3740:2019 and ANSI S12.51–2002).

In aeroacoustics, sound power calculations began as far back as Lighthill (1952), who developed general expressions for the acoustic intensity radiated by a turbulent jet, with the sound power being the integral of the intensity flux across a closed sphere. His development established important connections between the velocity of a jet, u, and its radiated power, most notably that the power scales by u^8 for subsonic jets. For supersonic jets, Ffowcs Williams (1963) showed that the sound power scales as u^3. Nagamatsu *et al.* (1969) used a laboratory-scale jet covering a range of subsonic and supersonic exit velocities to confirm these relationships and further explore spatial and spectral source properties of the radiated power. In cases when flow data are available, Eftekharian *et al.* (2023) proposed a matrix-based approach to the sound power using the Lighthill stress tensor. Their method identifies the radiating components of the stress tensor, which are qualitatively similar to structural radiation modes, and sums up the individual contributions. Their method was validated and applied to collections of vortices at various Mach numbers. For full-scale jet sources, Christian *et al.* (2023) used far-field measurements of a T-7A jet to determine overall sound power levels as a function of engine power. A follow-up study by Pratt *et al.* (2025) computed frequency-dependent sound power levels and provided a comparison between full-scale military aircraft and rockets. Sound power has also been featured prominently in rocket noise studies (e.g., McInerny, 1992; Lubert *et al.*, 2022; Kellison and Gee, 2023).

For sound power calculations in structural acoustics, some methods divide the radiated intensity into active (supersonic) and passive (subsonic) components. The active component radiates to the far-field, while the passive component evanesces (Williams, 1995). In this light, the sound power can be computed by determining the active intensity while ignoring the passive components; the standard surface integral can then be evaluated as normal. To this end, a number of analytic filtering schemes have been developed to determine these components, including a wavenumber decomposition (Williams, 1998) and spatially using convolutions (Fernandez-Grande *et al.*, 2012). In cases where the system geometry becomes complex, numerical schemes are available (see Correa and Tenenbaum, 2013, and Ferreira *et al.*, 2019). A related method called the nonnegative intensity divides the structure into radiation modes and computes the sound power based on the mode shape (Liu *et al.* 2016).

Another approach to calculating the acoustic field properties is to approximate the radiator with an equivalent source model (ESM). In structural acoustics, vibrating panels are commonly represented by a collection of elementary

[a]Email: to232@byu.edu

https://doi.org/10.1121/10.0042361

radiators. The velocity distribution of each of these radiators can be measured using techniques such as scanning laser doppler vibrometry (Rothberg *et al.*, 2017), then a radiation resistance matrix matching the surface geometry can be used to convert the velocity to sound power (Bates *et al.*, 2022). For more challenging geometries where the radiation resistance matrix becomes overly complex, other "lumped-element" style approaches become necessary. Fahnline and Koopmann (1996) suggested that when an object is divided into smaller elementary radiators, one can use the average volume velocities and pressures across each surface to solve the boundary value problem presented by the Kirchoff–Helmholtz integral theorem. This approach allows for accurate approximations without requiring excessive details about the surface. Fritze *et al.* (2009) expanded on this method and validated it against other methods of sound power for a diesel engine. An indirect method has also been explored by Bacon *et al.* (2023). One approach from active noise control (ANC) takes advantage of mutual coupling effects to calculate the sound power directly from the source configuration (Nelson *et al.*, 1987; Elliott *et al.*, 1991). The final expression makes use of the radiation resistance matrix and forms the foundation for the methods used in structural acoustics.

One drawback to these approaches is when noise sources couple only weakly or not at all. This happens when a noise field is generated by multiple unrelated sources, when there is extraneous noise in the system, or when the amplitude and phase relationships between sources change in time or space. The degree to which a field interacts is measured by its coherence. Perfectly coherent interactions allow for constructive and destructive interference and provide the base assumption in ANC. On the other hand, for incoherent interactions, there is no constructive or destructive interference, and total field properties can be calculated by summing over the radiation from each contributing source. While the role of coherence is most frequently seen in the context of signal processing and data analysis, it is less commonly emphasized in theoretical or analytical derivations. Jacobsen (1989) considers the complex intensity of an acoustic field and develops the coherence relationship between the sound pressure and particle velocity. In this case, the coherence becomes a strong indicator of whether a given field is created by one or multiple sources. Li *et al.* (1998) use this relationship to develop expressions for other energetic quantities of a partially coherent field, such as the kinetic and potential energy densities. They also identify that partially coherent interactions are scaled by the linear coherence between the two fields, which is notable for the current application. Using these principles, they develop a method for estimating field properties from a collection of partially coherent sources.

While partially coherent sources are plentiful, there is relatively little work discussing the explicit impact of coherence on field radiation properties. This paper combines the coherence relationships from Li *et al.* (1998) with the sound power approach from Nelson *et al.* (1987) to develop a generic expression for calculating the sound power from a collection of partially coherent monopoles. The expression is then validated analytically against a quadrupole-like source configuration with varying degrees of coherence. The limitations and use cases of this method are then explored with a simulated plate driven by a partially coherent source. Finally, the method is applied to experimental data from a turbulent jet. It is shown that when a system's coherence length is greater than about one wavelength, the source can be treated as coherent when calculating the sound power. Experimentally, this new source-based approach closely matches sound power calculations computed from far-field measurements.

II. COHERENCE

Consider two time signals, x and y, which are each a measurement of an acoustic field. The coherence between the two is a spectral quantity defined by

$$\gamma_{xy}^2 = \frac{|G_{xy}|^2}{G_{xx}G_{yy}}, \tag{1}$$

where $G_{xy} = \langle \hat{x}^* \hat{y} \rangle$ is the cross-spectrum between the signals and G_{xx} and G_{yy} are the respective autospectra (Bendat and Piersol, 1987). The Fourier transform is denoted by $\hat{\cdot}$, the complex conjugate by $(\cdot)^*$ and $\langle \cdot \rangle$ is the expectation value. The coherence is bounded by $0 \leq \gamma_{xy}^2 \leq 1$ and is a measure of how much of the spectral energy in y is related to the spectral energy in x. A value of 1 does not mean that the signals are identical in the time domain, just that there is a linear relationship between their autospectra, e.g., $G_{xx} = H_{xy}^2 G_{yy}$ for some transfer function H_{xy}. By extension, when two signals are partially coherent, $\gamma_{xy}^2 < 1$, only a portion of the energy in x is related to y, which can indicate a nonlinearity in a system, the presence of extraneous noise, or that the signal y is a composite of multiple signals beyond x (Bendat and Piersol, 1987). An additional representation of coherence comes in the form of the complex coherence, defined as $\gamma_{xy} = |\gamma_{xy}| e^{-j\theta_{xy}}$ where $|\gamma_{xy}| = +\sqrt{\gamma_{xy}^2}$ is the linear coherence and θ_{xy} is the phase angle of G_{xy} (Bendat and Piersol, 1987).

In some applications, the field coherence can be defined at a single point by replacing the time signals x and y with the pressure and vector particle velocity time series at that field location. This expression has a useful connection to energetic field quantities, such as the complex acoustic intensity and the kinetic and potential energy densities, as discussed by Jacobsen (1989). Li *et al.* (1998) used this work to establish connections to the underlying sources. In their work, Eq. (1) is used to calculate the coherence between the ith and jth sources based on the time series of their amplitudes, which are assumed to be stationary random processes. Given a partially coherent source description, the resultant energetic field quantities can be computed by considering pressure or particle velocity interactions between

each pair of sources and summing the contributions from each pair (including self-interactions). Importantly, the cross-terms are scaled by the linear coherence between the sources.

In practice, the source amplitude time series is neither given nor computed, but rather, a source coherence is simply defined. This is most prevalent in a cross-spectral ESMs, where underlying sources are not time resolved, but rather amplitudes are assigned to recreate the measured time-averaged spectra. The assumption throughout this paper is that the coherence between two sources is an inherent or defined property and that all field quantities are time-averaged versions of their corresponding stationary random process.

III. PARTIALLY COHERENT SOUND POWER

It is generally known from introductory physical acoustics that the sound power radiated by a general source is calculated by integrating the intensity flux through a closed surface containing the source, i.e., $\Pi = \oint_S \boldsymbol{I} \cdot d\boldsymbol{S}$. The acoustic intensity is taken as $\boldsymbol{I} = (1/2)\,Re\{p^*\boldsymbol{u}\}$ where p^* is the complex conjugate of the acoustic pressure, and $\boldsymbol{u}$ is the acoustic particle velocity. Both are functions of position and frequency rather than time. Note that the hat notation $(\hat{\cdot})$ has been dropped for frequency-dependent quantities for convenience and consistency with the literature. Since exact expressions of p and $\boldsymbol{u}$ can become unwieldy for sources more complicated than a monopole, it is common to make the acoustic far-field assumption (i.e., $kr \gg 1$), where the wavefronts can be approximated as planar. For such a wave, p and $\boldsymbol{u}$ are related by the specific acoustic impedance, $\rho c = p/|\boldsymbol{u}|$ and the acoustic intensity is approximated as $\boldsymbol{I} = (|p|^2/2\rho c)\boldsymbol{n}$, where $\boldsymbol{n}$ is the unit vector perpendicular to the wavefront. This significantly reduces the complexity of the problem since the far-field pressure is generally straightforward to calculate. This far-field method has considerable use for numerical sources since the far-field pressure of an arbitrary source configuration can be calculated at a closed surface via the Rayleigh integral, and the sound power quickly follows without needing to compute the derivatives required to construct $\boldsymbol{u}$.

An alternative sound power calculation that does not rely on the far-field approximation was presented by Nelson *et al.* (1987) for application in ANC. Their basic process is extended here to account for partially coherent interactions between sources. Consider a collection of N acoustic monopoles, such as those in Fig. 1, with complex source strengths (volume velocities) $\boldsymbol{q} = [q_1, \ldots, q_N]^T \in \mathbb{C}^N$ and positions $\boldsymbol{r}_i$. The sound power from the ith monopole can then be calculated by integrating across a surface enclosing the source,

$$\Pi_i = \frac{1}{2}\oint_S Re\{p_i^*\boldsymbol{u}_i\} \cdot d\boldsymbol{S}, \tag{2}$$

where p_i is the pressure at the surface of the ith monopole, including contributions from all the other monopoles and $\boldsymbol{u}_i$ is the total particle velocity at the source. Using properties of the Helmholtz equation, Nelson *et al.* (1987) showed that the particle velocity can be directly related to the source strength and the sound power computed as

$$\Pi_i = \frac{1}{2}Re\{p_i^* q_i\}. \tag{3}$$

The total sound power can then be calculated as the inner product between the vector of pressures at each source, $\boldsymbol{p} = [p_1, \ldots, p_N]^T$, and the source strengths,

$$\Pi = \frac{1}{2}Re\{\boldsymbol{p}^H\boldsymbol{q}\}, \tag{4}$$

where $(\cdot)^H$ is the Hermitian transpose. The pressure on one monopole due to all the others can be calculated using the relationship $\boldsymbol{p} = \boldsymbol{Z}\boldsymbol{q}$, where $\boldsymbol{Z}$ is the complex radiation impedance matrix (Elliott *et al.*, 1991) that operates on a set of source strengths and determines the pressure at each of the other sources (see Fig. 1). This matrix is symmetric, and its form is frequency and geometry dependent. Making this substitution into Eq. (4) yields the following:

$$\Pi = \frac{1}{2}Re\{\boldsymbol{q}^H\boldsymbol{Z}^H\boldsymbol{q}\}. \tag{5}$$

Equation (5) represents a key result from Nelson *et al.* (1987) and acts as the foundation for ANC applications such as fan noise reduction (Gee and Sommerfeldt, 2004) and in power measurements for structural acoustics (Bates *et al.*, 2022).

At this point, the partial coherence between sources needs to be accounted for. Li *et al.* (1998) showed that interactions between partially coherent fields are scaled by the linear coherence between their sources. Since it is the radiation impedance matrix in Eq. (5) that governs interactions between the sources, it is reasonable to introduce the partially coherent impedance matrix, $\boldsymbol{Z}_\gamma$, which has matrix elements $\boldsymbol{Z}_{\gamma_{ij}} = \boldsymbol{Z}_{ij}|\gamma_{ij}|$ where $|\gamma_{ij}| = +\sqrt{\gamma_{ij}^2}$ is the linear coherence between sources i and j. To emphasize that the power is computed from a partially coherent source, the notation for power is also updated to Π_γ. These substitutions are now made for the rest of the derivation.

Using the fact that $Re\{z\} = (1/2)(z + z^*)$ for any $z \in \mathbb{C}$, Eq. (5) becomes

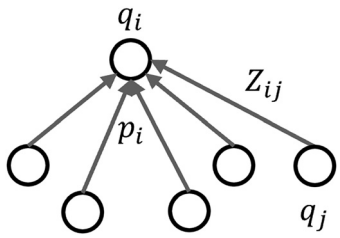

FIG. 1. Sample source configuration identifying the key components of the sound power derivation. Labels are q_i for the ith source strength, p_i is the total pressure on the ith source due to all sources, and Z_{ij} is the complex conversion factor that determines the pressure at the ith source due to q_j.

https://doi.org/10.1121/10.0042361

$$\Pi_\gamma = \frac{1}{4}\left(\boldsymbol{q}^H \boldsymbol{Z}_\gamma^H \boldsymbol{q} + \boldsymbol{q}^T \boldsymbol{Z}_\gamma^T \boldsymbol{q}^*\right). \tag{6}$$

Furthermore, since Π_γ is a scalar, each term in Eq. (6) is individually a scalar and equal to its own transpose, $\boldsymbol{q}^T \boldsymbol{Z}_\gamma^T \boldsymbol{q}^* = \boldsymbol{q}^H \boldsymbol{Z}_\gamma \boldsymbol{q}$. Making this substitution and factoring out $\boldsymbol{q}$ gives

$$\Pi_\gamma = \frac{1}{4}\left(\boldsymbol{q}^H \left(\boldsymbol{Z}_\gamma^H + \boldsymbol{Z}_\gamma\right)\boldsymbol{q}\right). \tag{7}$$

Noting that $\boldsymbol{Z}_\gamma$ is symmetric, $\boldsymbol{Z}_\gamma^H = \boldsymbol{Z}_\gamma^*$ and Eq. (7) can again be further reduced as follows:

$$\Pi_\gamma = \frac{1}{2}\boldsymbol{q}^H Re\{\boldsymbol{Z}_\gamma\}\boldsymbol{q}. \tag{8}$$

At this point, the radiation impedance matrix corresponding to the system needs to be specified. For monopoles in free space, the free-field radiation function is appropriate (Nelson *et al.*, 1987): $Z_{ij} = (jpck/4\pi\Delta r_{ij})e^{-jk\Delta r_{ij}}$, where $\Delta r_{ij} = ||r_i - \boldsymbol{r}_j||_2$ is the distance between sources i and j. The constants ρ and c are the ambient densities and sound speed, respectively, the parameter k is the acoustic wavenumber. Note that $Re\{\boldsymbol{Z}_{\gamma_{ij}}\} = (\rho ck^2/4\pi)sinc(k\Delta r_{ij})\gamma_{ij}$ and for the diagonal terms, $sinc(k\Delta r_{ii}) \to 1$ since $\Delta r_{ii} = 0$. Converting Eq. (8) from vector notation to a summation yields the expression,

$$\Pi_\gamma = \frac{\rho ck^2}{8\pi}\sum_{i,j} sinc\left(k\Delta r_{ij}\right)S_{ij} = \frac{\rho ck^2}{8\pi} sinc(k\boldsymbol{\Delta r}) : \boldsymbol{S}, \tag{9}$$

where : is the double dot product, and $S_{ij} = q_i^* q_j \gamma_{ij}$ is identified as the source cross-spectral matrix (CSM), which is a natural formulation for ESMs. Part of the elegance of Eq. (9) is that it is physically intuitive with respect to the sources, whereas the integral in Eq. (2) simply sums the intensity flux through a sphere. The diagonal elements identify the self-power generated from each source, while the off-diagonal elements indicate the power due to mutual coupling effects, including any *partially coherent* interactions. This expression is similar to what is found in other applications of the source sound power method (Bates *et al.*, 2022; Elliott and Johnson, 1993). The key difference here is that the power calculation is cast in a cross-spectral form, which is useful for analyzing partially coherent sources.

IV. APPLICATIONS

A. Analytical examples

To demonstrate that the expression for partially coherent sound power based on source strengths [Eq. (9)] yields the same results as the far-field process [Eq. (2)], the sound power is calculated both ways for a collection of four sources with varying degrees of coherence arranged at the corners of a square. Figure 2 shows the assumed source configuration. The monopoles have source strengths $\boldsymbol{q} = q[1, -1, 1, -1]^T$ and positions $\boldsymbol{r}_1 = (d/2)(1, 1, 0)$, $\boldsymbol{r}_2 = (d/2)(1, -1, 0)$, $\boldsymbol{r}_3 = (d/2)(-1, -1, 0)$, and $\boldsymbol{r}_4 = (d/2)(-1, 1, 0)$ in Cartesian space as shown in the diagram. A generic field location, $\boldsymbol{r}$, is included to define the spherical coordinates used in the far-field integration required for the calculation. Three cases are considered: first, the sources are assumed to be perfectly coherent (the standard quadrupole), then they are assumed to be incoherent, and finally, a partially coherent collection is analyzed by combining the two previous cases.

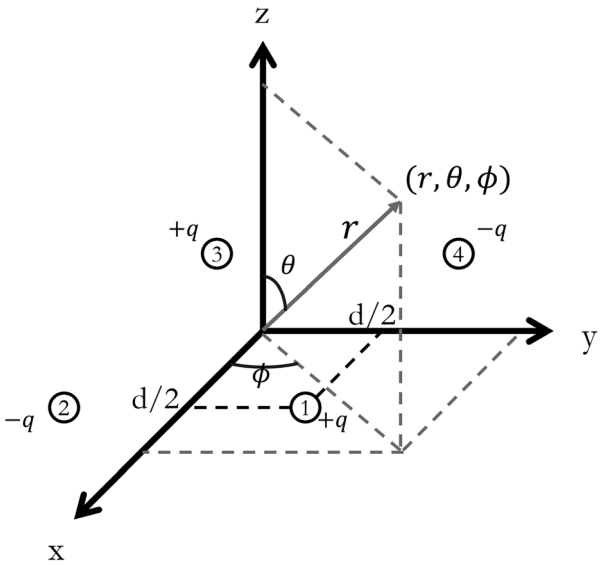

FIG. 2. Lateral quadrupole with indexed sources. A generic field point, denoted $\boldsymbol{r}$, is shown in spherical coordinates.

1. The standard quadrupole

Consider a generic field point located at (r, θ, ϕ) near the acoustic quadrupole in Fig. 2. The distance between the nth monopole and a location in the geometric far-field ($r \gg d$) can be approximated (Leishman, 2022) as $R_n \approx r - x_n \sin\theta\cos\phi - y_n \sin\theta \sin\phi$. The (free-field) pressure due to this monopole is given by $p_n(r, \theta, \phi) = (A_n/R_n)e^{-jkR_n}$ where the notation for acoustic amplitude, $A_n = j\rho ckq_n/4\pi$, has been introduced for convenience in the rest of the derivation. Since $r \gg d$, $R_n \approx r$ is a fine approximation for the amplitude as the second and third terms contribute relatively little to the final amplitude decay. However, the full expression is required for the phase since small changes can have a significant impact on pressure interactions. The total pressure field is simply the sum of the contributions from each source,

$$p(r, \theta, \phi) = \frac{A}{r}(e^{-jkR_1} - e^{-jkR_2} + e^{-jkR_3} - e^{-jkR_4}). \tag{10}$$

Plugging in each R_n and simplifying with trigonometric identities yields

$$p(r, \theta, \phi) = -\frac{4A}{r}e^{-jkr}\sin\left(\frac{kd}{2}\sin\theta\cos\phi\right) \times \sin\left(\frac{kd}{2}\sin\theta\sin\phi\right). \tag{11}$$

In anticipation of future integration, Eq. (11) is simplified by introducing the acoustic far-field assumption, $kd \ll 1$, which says that the source separation is small relative to an acoustic wavelength. Recall that $sinx \approx x$ for small x, and since the sine and cosine functions are at most 1, the approximation holds to give

$$p(r,\theta,\phi) \approx -\frac{A}{r} e^{-jkr} (kd)^2 \sin^2\theta \cos\phi \sin\phi. \tag{12}$$

The time-averaged intensity is then calculated as

$$\boldsymbol{I} = \frac{|A|^2 (kd)^4}{2\rho c r^2} \sin^4\theta \cos^2\phi \sin^2\phi \, \boldsymbol{n}, \tag{13}$$

where the $\boldsymbol{n}$ is the unit vector pointing away from the origin. The sound power follows next by evaluating the spherical integral

$$\Pi = \frac{|A|^2 (kd)^4}{2\rho c} \int_0^{2\pi} \int_0^{\pi} \sin^5\theta \cos^2\phi \sin^2\phi \, d\theta \, d\phi \tag{14}$$

$$= \frac{|A|^2 (kd)^4}{2\rho c} \left(\frac{16}{15}\right)\left(\frac{\pi}{4}\right), \tag{15}$$

$$\Pi = \frac{\rho c k^2}{120\pi} (kd)^4 |q|^2. \tag{16}$$

While the last two steps are straightforward, the hardest part is creating an integrable expression for the intensity, which is why the far-field assumption is convenient for most source arrangements.

On the contrary, the sound power for the same configuration is now evaluated directly from the sources. Given the source description, it is straightforward to create the two matrices required for the summation,

$$\boldsymbol{S} = |q|^2 \begin{bmatrix} 1 & -1 & 1 & -1 \\ -1 & 1 & -1 & 1 \\ 1 & -1 & 1 & -1 \\ -1 & 1 & -1 & 1 \end{bmatrix},$$

$$\boldsymbol{\Delta r} = d \begin{bmatrix} 0 & 1 & \sqrt{2} & 1 \\ 1 & 0 & 1 & \sqrt{2} \\ \sqrt{2} & 1 & 0 & 1 \\ 1 & \sqrt{2} & 1 & 0 \end{bmatrix}. \tag{17}$$

Taking advantage of the matrix symmetries, the complete summation is only composed of three terms: the self-power (diagonal elements), the mutually induced power from the sources that are diagonal to each other ($\sqrt{2}$ terms in $\boldsymbol{\Delta r}$), and the mutually induced power from each source's nearest neighbors (1 in $\boldsymbol{\Delta r}$). The sound power is then calculated as

$$\Pi_\gamma = \frac{\rho c k^2}{2\pi} |q|^2 \left(1 + \mathrm{sinc}\left(kd\sqrt{2}\right) - 2\mathrm{sinc}(kd)\right). \tag{18}$$

Equation (18) is more exact than the far-field expression [Eq. (16)] and is significantly easier to compute. To show that it collapses accordingly, let $kd \ll 1$ (the acoustic far-field assumption) and recall that $sinc\, x \approx 1 - x^2/3! + x^4/5!$. The sound power is then expressed as

$$\Pi_\gamma \approx \frac{\rho c k^2}{2\pi} |q|^2 \left(1 + 1 - \frac{2(kd)^2}{3!} + \frac{4(kd)^4}{5!} - 2 + \frac{2(kd)^2}{3!} - \frac{2(kd)^4}{5!}\right), \tag{19}$$

$$\Pi_\gamma = \frac{\rho c k^2}{120\pi} (kd)^4 |q|^2. \tag{20}$$

For significantly less work, the same expression is recovered using the Nelson *et al.* (1987) approach.

2. Incoherent sources

The same procedure is now applied to the same source arrangement, but with the assumption that each monopole radiates incoherently. In terms of the analytic derivation, the primary difference comes in the calculation of intensity. Recall that for coherent sources, $|p|^2 = |p_1 + p_2|^2$, while for incoherent sources $|p|^2 = |p_1|^2 + |p_2|^2$. Thus, the p^2 term in the intensity formula is instead calculated as

$$|p|^2 = \sum_{n=1}^{4} p_n p_n^*, \tag{21}$$

$$= \sum_{n=1}^{4} \frac{A_n}{r} e^{-jkR_n} \frac{A_n^*}{r} e^{jkR_n}, \tag{22}$$

$$|p|^2 = \frac{4|A|^2}{r^2}. \tag{23}$$

Note that Eq. (22) uses the pressure as seen in the geometric far-field, which simplifies the expression by ignoring any slight pressure differences due to the sources being off-center. Said another way, an observer in the geometric far-field sees the four monopoles as being co-located, and there is no angular component to their radiation. Additionally, since the monopoles radiate incoherently, there is no phase interaction, and the resultant pressure is identical to the case of a single monopole with four times the source strength. Computing the intensity and then the sound power is straightforward,

$$\boldsymbol{I} = \frac{2|A|^2}{\rho c r^2} \boldsymbol{n}, \tag{24}$$

$$\Pi = \frac{2|A|^2}{\rho c} \int_0^{2\pi} \int_0^{\pi} \sin\theta \, d\theta \, d\phi, \tag{25}$$

$$\Pi = \frac{\rho c k^2 |q|^2}{2\pi}. \tag{26}$$

https://doi.org/10.1121/10.0042361

When calculating the sound power using Eq. (9), the matrix $\boldsymbol{S}$ becomes $|q|^2$ times the identity matrix. This is because the cross-spectrum between each pair of sources becomes zero when there is no coherence [see Eq. (1)]. The distance matrix remains unchanged. Evaluating the summation yields the same expression as previously noted with virtually no effort,

$$\Pi_\gamma = \frac{\rho c k^2}{2\pi}|q|^2. \tag{27}$$

3. Partially coherent sources

To conclude, consider a superposition of the two previous examples. Since they must combine incoherently, the total source strength is given by summing the squared source strengths. Requiring that the total source strength be the same as the previous two examples yields the relationship $|q|^2 = |q_{coh}|^2 + |q_{inc}|^2 = \alpha|q|^2 + (1-\alpha)|q|^2$ for some parameter $0 \le \alpha \le 1$. The last equality is included to explicitly show how much coherent ($|q_{coh}|^2 = \alpha|q|^2$) and incoherent ($|q_{inc}|^2 = (1-\alpha)|q|^2$) energy is provided by each set. The cross-spectrum between the ith and jth source is calculated as

$$\begin{aligned} G_{ij} &= \langle q_i^* q_j \rangle = \langle (q_{coh_i} + q_{inc_i})^* (q_{coh_j} + q_{inc_j}) \rangle \\ &= \langle q_{coh_i}^* q_{coh_j} + q_{coh_i}^* q_{inc_j} + q_{inc_i}^* q_{coh_j} + q_{inc_i}^* q_{inc_j} \rangle \\ &= \alpha \langle q \rangle^2. \end{aligned} \tag{28}$$

The last equality holds because the cross-spectrum between two incoherent sources is, by definition, zero and only the coherent term remains. Similarly, the autospectrum for the i^{th} source is calculated as

$$\begin{aligned} G_{ii} &= \langle q_i^* q_i \rangle = \langle (q_{coh_i} + q_{inc_i})^* (q_{coh_i} + q_{inc_i}) \rangle \\ &= \langle q_{coh_i}^* q_{coh_i} + q_{coh_i}^* q_{inc_i} + q_{inc_i}^* q_{coh_i} + q_{inc_i}^* q_{inc_i} \rangle \\ &= \alpha \langle q \rangle^2 + (1-\alpha)\langle q \rangle^2 = \langle q \rangle^2. \end{aligned} \tag{29}$$

The coherence between any two sources is then given by Eq. (1) as a function of α

$$\gamma_{ij}^2 = \frac{\alpha^2 \left| \langle q \rangle^2 \right|^2}{\langle q \rangle^2 \langle q \rangle^2} = \alpha^2, \tag{30}$$

which identifies the parameter α as the linear coherence.

The sound power of this configuration is simple to compute using the far-field method. The total squared pressure is an incoherent sum of the squared pressures from each case,

$$p_{total}^2 = p_{coh}^2 + p_{inc}^2. \tag{31}$$

Since there are no cross-terms in the squared pressure, the total power can be computed as a linear sum of the power of each quadrupole,

$$\Pi_{total} = \Pi_{coh} + \Pi_{inc}. \tag{32}$$

Plugging in Eqs. (16) and (26) gives an expression for the total power

$$= \frac{\rho c k^2}{120\pi}(kd)^4 |q_{coh}|^2 + \frac{\rho c k^2}{2\pi}|q_{inc}|^2, \tag{33}$$

which is then simplified in terms of α as

$$\Pi_{total} = \frac{\rho c k^2}{2\pi}|q|^2 \left(\alpha \frac{(kd)^4}{60} + (1-\alpha) \right). \tag{34}$$

For the partially coherent method, the CSM is populated using Eq. (28) for the off-diagonal terms (accounting for different signs in the source description) and Eq. (29) for the main diagonal, while the distance matrix is the same as in Eq. (17),

$$\begin{aligned} \boldsymbol{S} &= \alpha|q|^2 \begin{bmatrix} 1/\alpha & -1 & 1 & -1 \\ -1 & 1/\alpha & -1 & 1 \\ 1 & -1 & 1/\alpha & -1 \\ -1 & 1 & -1 & 1/\alpha \end{bmatrix}, \\ \boldsymbol{\Delta r} &= d \begin{bmatrix} 0 & 1 & \sqrt{2} & 1 \\ 1 & 0 & 1 & \sqrt{2} \\ \sqrt{2} & 1 & 0 & 1 \\ 1 & \sqrt{2} & 1 & 0 \end{bmatrix}. \end{aligned} \tag{35}$$

The partially coherent sound power from these matrices is calculated as

$$\Pi_\gamma = \frac{\rho c k^2}{8\pi}\alpha|q|^2 \left(\frac{4}{\alpha} + 4\,sinc\left(kd\sqrt{2}\right) - 8\,sinc(kd) \right). \tag{36}$$

Making the same far-field approximation as in the coherent case simplifies Eq. (36) as follows:

$$\begin{aligned} \Pi_\gamma = \frac{\rho c k^2}{8\pi}\alpha|q|^2 \Bigg(&\frac{4}{\alpha} + 4 - \frac{8(kd)^2}{3!} + \frac{16(kd)^4}{5!} \\ &- 8 + \frac{8(kd)^2}{3!} - \frac{8(kd)^4}{5!} \Bigg), \end{aligned} \tag{37}$$

$$\Pi_\gamma = \frac{\rho c k^2}{2\pi}|q|^2 \left(\alpha \frac{(kd)^4}{60} + (1-\alpha) \right), \tag{38}$$

which is identical to Eq. (34). While not included here, this same procedure applies to systems of arbitrary coherence between monopoles. For the standard method, this would result in a summation like Eq. (32), where each term is the sound power from some partial source, essentially performing a partial field decomposition. The active and nonnegative intensity methods (Williams, 1995; Liu *et al.*, 2016) could also be applied to this situation; however, given that they assume a coherent source description, the same partial field decomposition approach would have to be applied. Given the usefulness of these methods, it would be beneficial to explore how partial

coherence impacts the supersonic wavenumbers, but that is beyond the scope of this paper. The partially coherent sound power approach sidesteps this added complication by accounting for the coherence directly in the description of $\boldsymbol{S}$. It should be noted that due to the matrix formulation of this approach, numerical power calculations using this method are faster than other forms of numerical far-field integration.

B. Example systems

Following the previous validation discussion, it is important to discuss what types of partially coherent systems benefit the most from this method. For systems beyond simple point sources, there are two components in the partially coherent sound power that drive off-diagonal terms to zero. The first of these is the coupling distances between sources, and the second is the natural coherence lengths present in the system. Both will be discussed in the remainder of the paper.

From Eq. (9), the coupling distance between sources is governed by the $sinc(k\Delta r_{ij})$ term. Due to the oscillatory nature of the *sinc* function, it is difficult to prescribe an exact distance over which sources couple. However, in the work surrounding this paper, we have found that $k\Delta r \approx 2\pi$, or $\Delta r \approx \lambda$ appears to be a good cutoff. This distance captures the first two cycles of the *sinc* function and captures about 90% of the total integrated value. Using this as a cutoff metric implies that interactions between sources separated by more than about one wavelength are negligible regardless of their coherence. The effect is a diagonal mask passed across the source CSM before the summation is executed. This coupling distance is most important relative to the system's coherence length, L_{γ^2}, which is the distance across which the coherence is greater than 0.5. When L_{γ^2} is greater than the coupling distance, excess coherence is ignored, and the sound power can be calculated as though the sources were perfectly coherent.

An important consideration when using the sound power calculation (and generally in acoustic modeling) is the discretization of the underlying sources. Generally, a functioning ESM is limited in frequency by the separation distance between underlying sources. From the Nyquist sampling theorem, a minimum of two sources per wavelength should be present to avoid aliasing. While this is important for accurate radiation, it is doubly important for computing the partially coherent sound power. In cases where there is an insufficient number of sources for a given frequency, the coupling distance drops below the source resolution, which has the effect of forcing each source to be treated independently, and coherence no longer matters.

The rest of this section explores two examples demonstrating the applicability of the partially coherent sound power. The first is an excited plate where equivalent sources are in close proximity and the characteristic coherence length is variable. The second example comes from jet noise measurements of a full-scale military aircraft, a naturally occurring partially coherent source.

1. Partially coherent plate

Consider a square vibrating plate that is modeled as a collection of elementary radiators by subdividing the domain into smaller regions, each of which can be assigned a displacement amplitude that directly relates to its acoustic source strength. The plate is driven in such a way that all points are excited equally, but with an inter-source coherence of $\gamma^2 = e^{-\ln(2)r/L_{\gamma^2}}$. With this model, the source CSM is given as $S_{ij} = |q|^2 e^{-\ln(2)r_{ij}/2L_{\gamma^2}}$. While such a scenario is a bit idealized, the source strength distribution and the coherence models can be replaced without impacting the key results presented here. One relevant example is flow-induced noise, such as on an airfoil or a fuselage. In these cases, the source strength distribution and coherence can be determined using something more realistic, such as the Corcos model (Corcos, 1963), see also Soranna *et al.* (2024). These have not been implemented here as the simpler model is more convenient for the purposes of this paper.

Returning to the vibrating plate, suppose the plate has a side length of $L = 0.5\,\text{m}$, discretized into 100 elementary

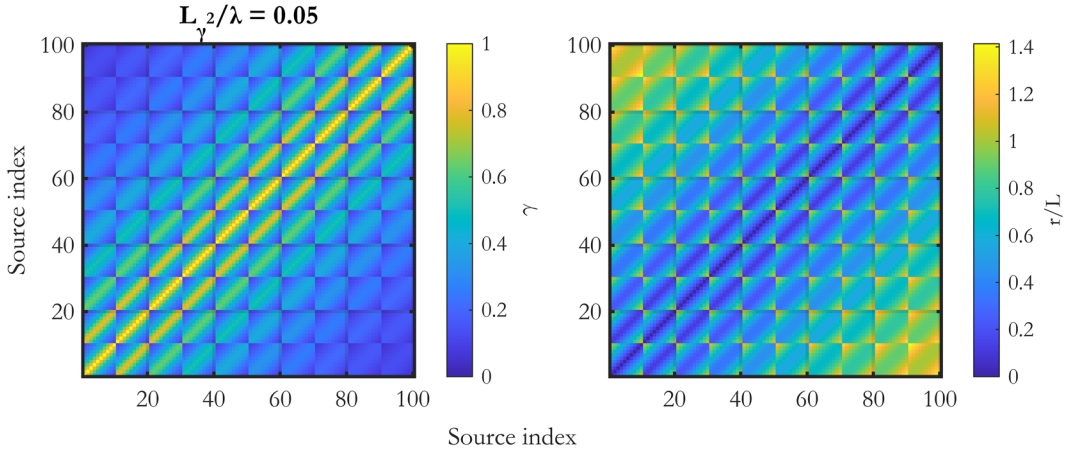

FIG. 3. Sample source CSM and distance matrix for partially coherent sound power calculations. The coherence length for this example is $L_{\gamma^2}/\lambda = 0.05$. The CSM has been normalized by source strength and the distance by plate side length.

https://doi.org/10.1121/10.0042361

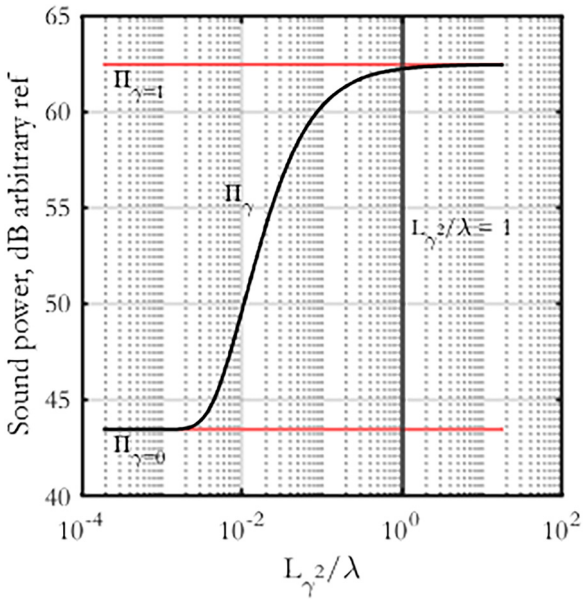

FIG. 4. Sound power as a function of normalized coherence length. The black curve shows the partially coherent sound power, while the red lines show the fully coherent and fully incoherent cases, respectively. A vertical line identifies the effective coupling distance.

radiators (5.5 cm spacing). The sound power of this configuration is computed using Eq. (9) for a range of coherence lengths at a frequency of 200 Hz. Figure 3 shows the $\boldsymbol{S}$ and $\boldsymbol{\Delta r}$ matrices for the configuration with a normalized coherence length of $L_{\gamma^2}/\lambda = 0.05$. This normalization by wavelength was chosen to remove the direct impact of the frequency on the sound power trends; as such, performing the same calculation at other frequencies results in qualitatively similar results. For ease of generalization, the CSM has been normalized by the squared source strength, resulting in a source map of the linear coherence. Similarly, the distance matrix has been normalized by the plate edge length to remove the impact of plate dimensions. Note that both are Toeplitz symmetric matrices, a feature common to plate measurements (Ebeling *et al.*, 2022).

The partially coherent sound power of this configuration is computed using Eq. (9) for a range of coherence lengths at a frequency of 200 Hz. For comparison purposes, the sound power is also computed assuming a perfectly coherent or incoherent source description. These results are plotted in Fig. 4 with the coherent and incoherent sound powers plotted in red and the partially coherent sound power in black. A vertical line is also included at $L_{\gamma^2}/\lambda = 1$ to denote the effective coupling distance between sources. At small normalized coherence lengths, the partially coherent sound power is approximated by the incoherent sound power. This approximation becomes valid because, as the coherence length becomes smaller, there is less interaction between sources, and it can be treated incoherently. At the other extreme, as coherence lengths increase beyond the coupling distance, the sound power can be approximated using a coherent source, even though the plate is not fully coherent. Between these two extremes is where partially coherent interactions are required when computing the sound power.

2. Military jet noise

The final application of the method involves a more complicated, experimental noise source: a jet produced by a T-7A installed GE-F404 engine, which represents a partially coherent noise source (Mathews and Gee, 2024). This experiment was conducted in the early hours of 18 August 2019, at Holloman Air Force Base in New Mexico, and featured over 200 microphones covering the acoustic near and far fields. The near field was sampled at 204.8 kHz by an array of 120 GRAS 46BD and 46BG ¼" (GRAS, Holte, Denmark) pressure microphones. The array used for this analysis is shown in Fig. 5 and plotted as a function of nozzle diameter (D). The array ran parallel to the jet centerline in the forward direction and then parallel to the expected shear layer downstream of the nozzle. Each microphone was taped to the ground to help mitigate ground reflections. The inter-element spacing varied across the array, with smaller intervals near the sideline and larger spacing at the far downstream segment of the array. Due to the nature of the array, aliasing begins to occur at a spatial Nyquist frequency

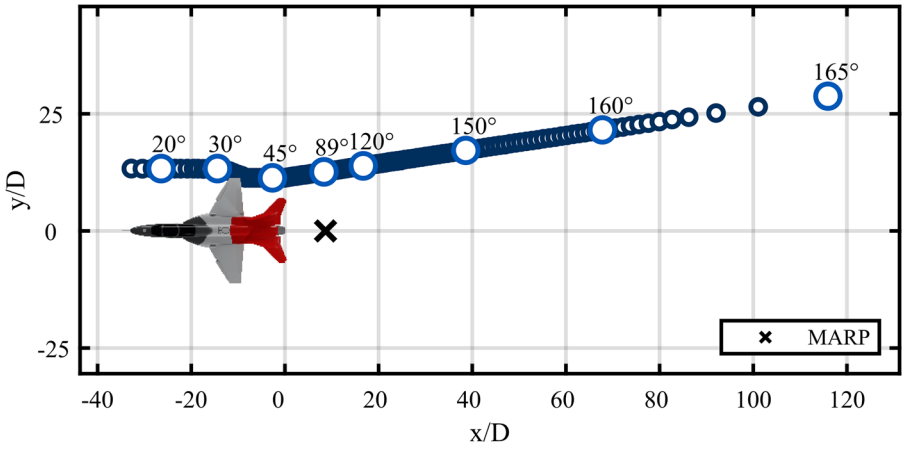

FIG. 5. Schematic of the T-7A imaging array. A few inlet angles are shown relative to the MARP to demonstrate the angular span of the near-field measurement.

of about 500 Hz, though this is addressed later. Inlet angles relative to the microphone array reference point (MARP) at various microphone positions have been highlighted to demonstrate the angular span of the near-field measurement. This same array has been used in several other studies on jet noise source characterization of this military aircraft (Olaveson and Gee, 2024; Mathews and Gee, 2024; Gee *et al.*, 2025). The far-field was measured using five arcs at 19, 38, 76, 152, and 229 m, centered on the MARP and elevated five feet off the ground. This validation compares sound power calculations using the near-field data to those made using the 38 and 76 m arcs as processed by Pratt *et al.* (2025)

The aircraft was cycled through six engine conditions, ranging from idle to full afterburner (AB), including military power (MIL), or 100% thrust. Each condition was held long enough to allow for at least 30 s of steady-state data. Each run-up was repeated six times to allow for broader averaging. Further details on this measurement can be found in Leete *et al.* (2021).

Spectral data collected by the imaging array were processed from the 30 s recordings for frequencies ranging from 3 to 1000 Hz with a 3 Hz resolution and compiled into CSMs. Since this includes frequencies beyond the spatial Nyquist frequency, each CSM is interpolated using UPAINT (unwrapped-phase array interpolation) as in Mathews and Gee (2024), which has been shown to effectively reduce aliasing features (such as grating lobes) while maintaining fidelity to the measured field. For each frequency, an ESM is created using the hybrid beamforming (HM) method as presented by Padois *et al.* (2014) and applied to this same T-7A dataset by Olaveson and Gee (2025). The HM method uses measured CSMs to solve the regularized inverse problem for the complex source strengths of a collection of monopoles at presumed locations, allowing for partially coherent interactions between all sources. The result is a cross-spectral representation of the noise source. For this application, each ESM is cast onto a set of monopoles along the jet centerline ranging from about −6 to 65D relative to the nozzle exit with an inter source spacing of 0.2D as shown in the left panel of Fig. 6. This spacing is dense enough to capture the wavelengths of the desired frequencies and the aperture is large enough to smoothly taper source strengths to zero at the edges for all frequencies. Note that the spatial limits in Fig. 6 are reduced from the full ESM to better emphasize the relevant sources. To account for ground reflections caused by the rigid ground, an identical set of monopoles is included beneath the aircraft to act as an image source. After the HM processing is complete, the image sources are removed for the rest of the analysis to simulate a free-field environment. The right panel of Fig. 6 shows a colormap of the free-field source CSM. The partially coherent nature of the noise source can be seen by the vanishing nature of the off-diagonal elements, which shows that sources are only coherent with those nearest themselves. There are other interesting coherence features present in this source CSM, but these will not be discussed here. Instead, the reader is directed to Mathews and Gee (2024) for a more involved discussion on the coherence properties of the T-7A jet.

Figure 6 contains all the information needed to evaluate the partially coherent sound power, which is done for each frequency and then compiled into a single sound power spectrum. For comparison purposes, the sound power is also calculated using a fully coherent and a fully incoherent source model.

For this same measurement, Christian *et al.* (2023) and Pratt *et al.* (2025) used two far-field arcs to determine overall and frequency-dependent sound power levels. Their approach assumes that the source can be treated as axisymmetric and that the intensity can be calculated using a far-field approximation. The pressure measurements at the far-field arcs then constitute a representative slice of the pressure field, which can then be used to construct a closed surface around the jet. Ground reflections are handled using an

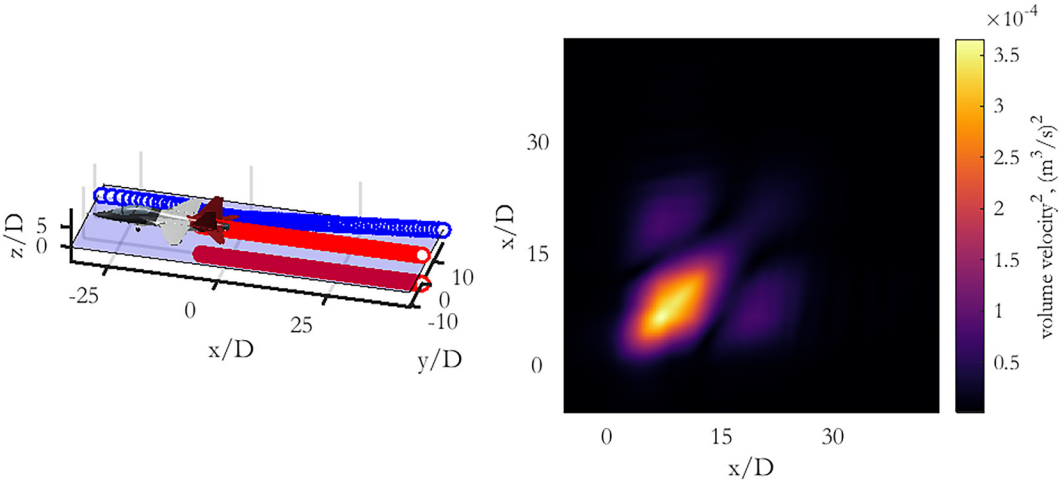

FIG. 6. Left, the distribution of reconstructed source locations for the beamforming. The array beneath the aircraft acts as an image source, which is then removed in the rest of the processing to simulate a free-field environment. Right, a colormap of a sample ESM at 201 Hz, which represents a peak frequency. The spatial limits for this example have been reduced to focus on the prominent sources.

https://doi.org/10.1121/10.0042361

empirical model that accounts for atmospheric turbulence and finite ground impedance, proposed by Daigle (1979) and implemented for extended noise sources by Gee *et al.* (2014). For further details on how the ground reflections are handled in this case, the reader is directed towards Christian *et al.* (2022)

Figure 7 compares the sound power calculated from the ESM to the measured sound power for both MIL (left) and AB (right). Included in the upper left corner is the overall sound power level (OAPWL) calculated using the HM results. Christian *et al.* (2023) showed that the OAPWL for the T-7A is between 167.7 and 170.5 dB re 1 pW for MIL and between 172.1 and 174.1 dB for AB. From the HM, the OAPWL is calculated as 168.3 dB at MIL and 173.3 dB at AB, which fits within the ranges of the experimental data.

Each plot in Fig. 7 contains two primary sound power spectra: one from the HM-derived source and one for the measured T-7A sound power spectra. In addition to these are two fainter curves in red corresponding to the fully coherent and fully incoherent sound powers that act as limiting cases. The T-7A spectrum is an average of the two sound power spectra taken at the 38 m and 76 m far-field arcs from Pratt *et al.* (2025). Frequencies above 500 Hz have been greyed out to indicate that the HM relies on an interpolated CSM beyond the spatial Nyquist frequency. For MIL (left), the two curves are in generally good agreement up to about 500 Hz where the HM curve misses the peak in the T-7A spectrum by a little less than 1 dB. Beyond this point, the high-frequency slopes diverge.

Some of the slope disagreement has to do with the ground reflection model implemented by Pratt *et al.* (2025). Their model assumes that the ground reflection can be modeled as a partially coherent interaction with the ground. While their approach is justifiable and has been validated, their results still show evidence of a ground reflection null at around 1 kHz. The effect is that the spectral slope decreases much faster than it should leading up to those frequencies, which is observed in Fig. 7. From Eldred (1971), the high-frequency spectral slope is expected to decay at a rate of $1/f^2$, or 20 dB per decade on a log-log scale. The Pratt *et al.* (2025) high-frequency slope is more than 30 dB per decade. On the contrary, the sound power computed using the beamforming has a spectral slope of about 13 dB per decade at MIL. Neither spectral slope is quite right, but the implication is that the true sound power exists somewhere between these two curves, and most likely closer to the beamformed results. The beamforming overprediction is likely a limitation in the signal processing, despite the application of UPAINT. It is possible that during the phase unwrapping and interpolation, the coherence between measured signals is artificially inflated, which would lead to more energy at the higher frequencies.

The results at AB (right) are comparable to those of MIL and exhibit the same spectral slope disagreement discussed previously.

The other feature in Fig. 7 is the comparison between the incoherent, partially coherent, and fully coherent sound power spectra. As noted in Sec. IV B 1, partially coherent interactions become unimportant when the coherence lengths are much longer than the coupling distance, and the entire system can be treated as coherent when determining the sound power. From the similarity between the fully coherent model and the partially coherent one, it becomes clear that this is true for the high-frequency radiation of the T-7A jet. While it is well known that the jet coherence length decreases with increasing frequency (Swift *et al.*, 2018), the coupling distance decreases faster, such that for frequencies above a few hundred Hz, $L_{\gamma^2} > \lambda$ holds and the source can be approximated as coherent. At frequencies below about 200 Hz, which is still within the peak radiation region, partially coherent interactions are important to the source description.

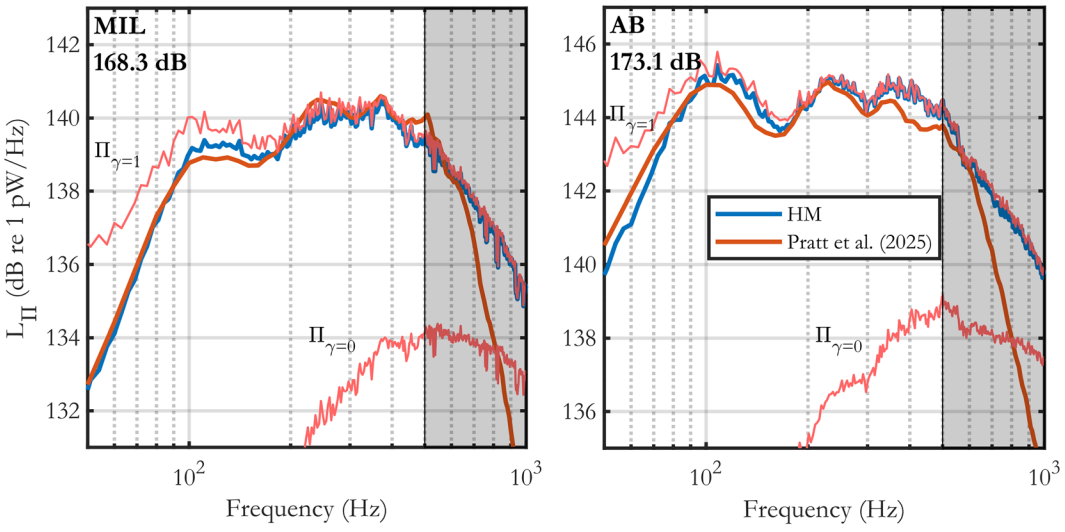

FIG. 7. Sound power spectra calculated from the Hybrid Method ESM compared to spectra from the measured far-field data after correcting for ground reflections. The overall sound power level calculated from the beamforming is included in the top left of each plot. The greyed-out region on the right indicates frequencies above the spatial Nyquist frequency where the HM processing relies on interpolation. Two red curves identify the sound power computed with a fully coherent and a fully incoherent source model.

The incoherent source model is virtually never a good model for the source, though the trend suggests that the three methods converge at sufficiently high frequencies. This is less of a limiting behavior and more of an indication that, at higher frequencies, the density of the beamforming array is insufficient to describe the noise source.

V. CONCLUSION

This paper extends the formulation of Nelson *et al.* (1987), who demonstrated that the sound power radiated by an arbitrary collection of monopoles can be computed using a radiation resistance matrix that captures mutual coupling between sources. Using a key result from Li *et al.* (1998), that the interaction between acoustic sources is scaled by their linear coherence, the partial coherence is incorporated into this framework. It is shown that the coherence appears as a minor scaling term that can be included in the radiation resistance matrix. If the sources are instead compiled into a CSM, which is a natural representation for many ESMs, the total power becomes a simple double summation. The utility of this approach is demonstrated by computing the sound power from a lateral quadrupole using the standard far-field method versus the matrix approach. This example highlights the impact of partial coherence on the radiated sound power and the simplicity of this new method. Other sound power methods, such as the supersonic intensity, could also be extended to account for partially coherent interactions. Such an extension would likely provide physical insights into how coherence impacts structural radiation modes.

While this method is valid, there are two factors that work to suppress off-diagonal source interactions: the coupling distance and the coherence length. Coupling between sources is a function of their separation distance. When sources are far apart with respect to a wavelength, there is minimal coupling and thereby no cross-term contributions from these sources. This effectively creates a mask over the source CSM that limits which cross-terms contribute to the overall power. The coherence length describes the physical distance over which sources are coherent. If the coherence length is smaller than the physical extent of the system, some sources will be incoherent with others, and their cross-terms do not contribute to the overall sound power. When the coherence length is larger than the coupling distance (about one wavelength), the masking effect dominates, and any excess coherence can be ignored. The result is that the same sound power can be calculated by assuming that all the sources in the model are perfectly coherent with each other. This relationship ($L_{\gamma^2} > \lambda$) provides an important metric for determining when partially coherent interactions are important to the radiated sound power.

To demonstrate these regimes, two examples are presented. The first is a plate that is excited by a partially coherent source with a characteristic coherence length, which is the case for turbulent flow over an airfoil and for structural vibrations induced by a jet or rocket plume. This numerical example varies the source coherence length and demonstrates the collapse of the partially coherent sound power to that of the fully coherent model. The second example uses noise data from a full-scale military jet to construct an ESM using hybrid beamforming (Padois *et al.*, 2014). The (free-field) sound power is calculated directly from the ESM and compared to the sound power calculated from far-field arcs at the same measurements. Both methods agree to within less than 1 dB below the spatial Nyquist frequency for MIL and AB operating conditions. Beyond this point, the high-frequency slopes diverge due to limitations in the beamforming processing and the ground reflection correction model used by Pratt *et al.* (2025). While one would expect a partially coherent jet to be the natural application of this method, it is also seen that partially coherent interactions are unimportant to the sound power at higher frequencies. The reason for this is that while the jet coherence lengths decrease rapidly with increasing frequency, the coupling distance decreases faster, pushing the jet into the coherent regime for all but the lowest frequencies.

In conclusion, this paper presents a succinct method for determining the sound power generated by a partially coherent source. While this method has been applied to a free-field environment, a different radiation resistance matrix can be used in Eq. (8) that better captures restrictions of a system that cannot be modeled as a free-field radiator. In these cases, the coupling distance restriction discussed in this paper will depend on the form of that matrix. Future applications of this method include turbulent flow over an airfoil, as discussed earlier, as well as low-frequency turbulent flows, such as noise radiation from rocket plumes. Additionally, since this derivation is based on the approach used in ANC, the application to noise control of a partially coherent source would be a natural project for future work. Other jet noise regimes should also be investigated, such as noise radiation from subsonic jets as well as consistency with other full-scale military aircraft.

ACKNOWLEDGMENTS

The authors gratefully acknowledge the funding provided by the Office of Naval Research under Grant No. N00014-21-1–2069 with project monitor Dr. Steven Martens, Code 351 Jet Noise Reduction. We would also like to thank the reviewers for their feedback, which helped improve the quality of this work.

AUTHOR DECLARATIONS

Conflict of Interest

The authors have no conflicts to disclose.

DATA AVAILABILITY

Data used in the validation analysis are available by request to the T-7A Program Office.

ANSI/ASA (**2012**). ANSI S12.51, *Determination of Sound Power Levels and Sound Energy Levels of Noise Sources using Sound Pressure – Precision Methods for Reverberation Test Rooms* (ANSI, New York).

Bacon, I. C., Jensen, N. M., Sommerfeldt, S. D., and Blotter, J. D. (**2023**). "Investigation of the radiated sound energy from noise sources using an

indirect vibration-based sound power approach," J. Acoust. Soc. Am **153**, A287.
Bates, T. P., Bacon, I. C., Blotter, J. D., and Sommerfeldt, S. D. (**2022**). "Vibration-based sound power measurements of arbitrarily curved panels," J. Acoust. Soc. Am **151**, 1171–1179.
Bendat, J. S., and Piersol, A. G. (**1987**). *Random Data*, 4th ed. (Wiley, Hoboken, NJ), Chap. 6.
Christian, M. A., Gee, K. L., Streeter, J. B., Wall, A. T., and Campbell, S. C. (**2022**). "Implementing a heuristic method to correct ground reflection efforts observed in full-scale tactical aircraft noise measurements," Proc. Mtgs. Acoust. **50**, 040005.
Christian, M. A., Gee, K. L., Streeter, J. B., Wall, A. T., and Campbell, S. C. (**2023**). "Sound power and acoustic efficiency of an installed GE F404 jet engine," JASA Express Lett. **3**, 073601.
Corcos, G. M. (**1963**). "Resolution of pressure in turbulence," J. Acoust. Soc. Am **35**, 192–199.
Correa, C. A., Jr., and Tenenbaum, R. A. (**2013**). "Useful intensity: A technique to identify radiating regions on arbitrary shaped surfaces," J. Sound Vib. **332**(6), 1567–1584.
Daigle, G. A. (**1979**). "Effects of atmospheric turbulence on the interference of soundwaves above a finite impedance boundary," J. Acoust. Soc. Am. **65**(1), 45–49.
Ebeling, J. C., Bacon, I. C., Bates, T. P., Sommerfeldt, S. D., and Blotter, J. D. (**2022**). "Improved efficiency of vibration-based sound power computation through multi-layer radiation resistance matrix symmetry," JASA Express Lett. **2**, 125601.
Eftekharian, E., Croaker, P., Marbug, S., Liu, D., and Kessissoglou, N. (**2023**). "Non-negative aeroacoustic source contributions to radiated sound power," J. Acoust. Soc. Am **153**, 3522–3531.
Eldred, K. M. (**1971**). "Acoustic loads generated by the propulsion system," Report No. NASA SP-8072 (NASA, Washington, DC).
Elliott, S. J., and Johnson, M. E. (**1993**). "Radiation modes and the active control of sound power," J. Acoust. Soc. Am **94**, 2194–2204.
Elliott, S. J., Joseph, P., Nelson, P. A., and Johnson, M. E. (**1991**). "Power output minimization and power absorption in the active control of sound," J. Acoust. Soc. Am. **90**, 2501–2512.
Fahnline, J. B., and Koopmann, G. H. (**1996**). "A lumped parameter model for the acoustic power output from a vibrating structure," J. Acoust. Soc. Am. **100**, 3539–3547.
Fernandez-Grande, E., Jacobsen, F., and Leclère, Q. (**2012**). "Direct formulation of the supersonic acoustic intensity in space domain," J. Acoust. Soc. Am. **131**, 186–193.
Ferreira, V. L. D., Tenenbaum, R. A., Dias, F. L., and Correa, C. A., Jr. (**2019**). "Power operator dimensional reduction to obtain the useful intensity in rectangular plates with several boundary conditions," J. Sound Vib. **448**, 130–145.
Ffowcs Williams, J. E. (**1963**). "The noise from turbulence convected at high speed," Philos. Trans. R. Soc. London, Ser. A: Math. Phys. Sci. **255**(1061), 469–503.
Fritze, D., Marburg, S., and Hardtke, H.-J. (**2009**). "Estimation of radiation sound power: A case study on common approximation methods," Acta Acust. united Ac. **95**, 833–842.
Gee, K. L., Neilsen, T. B., and James, M. M. (**2014**). "Including source correlation and atmospheric turbulence in a ground reflection model for rocket noise," Proc. Mtgs. Acoust **22**, 040001.
Gee, K. L., Olaveson, T. W., and Mathews, L. T. (**2025**). "Convective Mach number and full-scale supersonic jet noise directivity," AIAA J. **63**(4), 1393–1404.
Gee, K. L., and Sommerfeldt, S. D. (**2004**). "Application of theoretical modeling to multichannel active control of cooling fan noise," J. Acoust. Soc. Am. **115**, 228–236.
ISO (**2019**). ISO 3740, "Determination of sound power levels of noise sources" (ISO, Geneva, Switzerland).
Jacobsen, F. (**1989**). "Active and reactive, coherent and incoherent sound fields," J. Sound Vib. **130**(3), 493–507.
Kellison, M. S., and Gee, K. L. (**2023**). "Sound power of NASA's lunar rockets: Space Launch System versus Saturn V," JASA Express Lett. **3**, 113601.
Leete, K. M., Vaughn, A. B., Bassett, M. S., Rasband, R. D., Novakovich, D. J., Gee, K. L., Campbell, S. C., Mobeley, F. S., and Wall, A. T. (**2021**). "Jet noise measurements of an installed GE F404 engine," in *Proceedings of the AIAA SciTech Forum*, AIAA Paper 2021–1638.
Leishman, T. W. (**2022**). *Physics 660 Class Notes* (Department of Physics and Astronomy, Brigham Young University, Provo, UT).
Li, J.-F., Pascal, J.-C., and Carles, C. (**1998**). "Energy fields of partially coherent sources," J. Acoust. Soc. Am **103**, 962–972.
Lighthill, M. J. (**1952**). "On sound generated aerodynamically I. General theory," Proc. R. Soc. London, Ser. A: Math. Phys. Sci. **211**(1107), 564–587.
Liu, D., Peters, H., Marbug, S., and Kessissoglou, N. (**2016**). "Supersonic intensity and non negative intensity for prediction of radiated sound," J. Acoust. Soc. Am **139**, 2797–2806.
Lubert, C. P., Gee, K. L., and Tsutsumi, S. (**2022**). "Supersonic jet noise from launch vehicles: 50 years since NASA SP-8072," J. Acoust. Soc. Am. **151**, 752–791.
Mathews, L. T., and Gee, K. L. (**2024**). "Acoustical holography and coherence-based noise source characterization of an installed F404 engine," AIAA J. **62**(6), 2186–2199.
McInerny, S. A. (**1992**). "Characteristics and predictions of far-field rocket noise," Noise Control Eng. J. **38**(1), 5–16.
Nagamatsu, H. T., Sheer, R. E., and Horvay, G. (**1969**). "Supersonic jet noise theory and experiments," NASA SP-207 (NASA, Washington, DC).
Nelson, P. A., Curtis, A. R. D., Elliott, S. J., and Bullmore, A. J. (**1987**). "The minimum power output of free field point sources and the active control of sound," J. Sound Vib. **116**(3), 397–414.
Olaveson, T. W., and Gee, K. L. (**2024**). "Wavelet-based characterization of spatiospectrotemporal structures in F404 engine jet noise," AIAA J. **62**(11), 4399–4410.
Olaveson, T. W., and Gee, K. L. (**2025**). "Multiple wavepacket decomposition of F404 engine military jet noise," in *Proceedings of AIAA Aviation Forum and ASCEND*, Las Vegas, NV (July 21-25).
Padois, T., Gauthier, P.-A., and Berry, A. (**2014**). "Inverse problem with beamforming regularization matrix applied to sound source localization in closed wind-tunnel using microphone array," J. Sound Vib. **333**, 6858–6868.
Pratt, H. J., Mathews, L. T., Olaveson, T. W., and Gee, K. L. (**2025**). "Sound power level spectra of an installed General Electric F404 engine," JASA Express Lett. **5**, 043601.
Rothberg, S. J., Allen, M. S., Castellini, P., Maio, D. D., Dirckx, J. J. J., Ewins, D. J., Halkon, B. J., Muyshondt, P., Paone, N., Ryan, T., Steger, H., Tomasini, E. P., Vanlanduit, S., and Vignola, J. F. (**2017**). "An international review of laser Doppler vibrometry: Making light work of vibration measurement," Opt. Lasers Eng. **99**, 11–22.
Soranna, F., Heaney, P. S., Sekula, M. K., Piatak, D. J., and Ramey, J. M. (**2024**). "Comparison of Corcos-based experimentally derived coherence factors for buffet forcing function," J. Spacecr. Rockets **61**(1), 285–295.
Swift, S. H., Gee, K. L., Neilsen, T. B., Wall, A. T., Downing, J. M., and James, M. M. (**2018**). "Spatiotemporal correlation analysis of jet noise from a round-nozzle supersonic aircraft," in *Proceedings of the AIAA Aviation Forum*, Atlanta, GA (June 25-29).
Williams, E. G. (**1995**). "Supersonic acoustic intensity," J. Acoust. Soc. Am. **97**, 121–127.
Williams, E. G. (**1998**). "Supersonic acoustic intensity on planar sources," J. Acoust. Soc. Am **104**, 2845–2850.